We are IntechOpen,
the world's leading publisher of
Open Access books
Built by scientists, for scientists

4,800
Open access books available

122,000
International authors and editors

135M
Downloads

Our authors are among the

154
Countries delivered to

TOP 1%
most cited scientists

12.2%
Contributors from top 500 universities

CLARIVATE ANALYTICS
BOOK CITATION INDEX
INDEXED

WEB OF SCIENCE™

Selection of our books indexed in the Book Citation Index
in Web of Science™ Core Collection (BKCI)

Interested in publishing with us?
Contact book.department@intechopen.com

Numbers displayed above are based on latest data collected.
For more information visit www.intechopen.com

Chapter

Structural Phase Transitions of Hybrid Perovskites CH₃NH₃PbX₃ (X = Br, Cl) from Synchrotron and Neutron Diffraction Data

Carlos Alberto López, María Consuelo Alvarez-Galván,
Carmen Abia, María Teresa Fernández-Díaz and
José Antonio Alonso

Abstract

Methylammonium (MA) lead trihalide perovskites, that is, CH₃NH₃PbX₃ (X = I, Br, Cl), have emerged as a new class of light-absorbing materials for photovoltaic applications. Indeed, since their implementation in solar-cell heterojunctions, they reached efficiencies above 23%. From a crystallographic point of view, there are many open questions that should be addressed, including the role of the internal motion of methylammonium groups within PbX₆ lattice under extreme conditions, such as low/high temperature or high pressure. For instance, in MAPbBr₃ perovskites, the octahedral tilting can be induced upon cooling, lowering the space group from the aristotype $Pm\bar{3}m$ to $I4/mcm$ and $Pnma$. The band gap engineering brought about by the chemical management of MAPb(Br,Cl)₃ perovskites has been controllably tuned: the gap progressively increases with the concentration of Cl ions from 2.1 to 2.9 eV. In this chapter, we review recent structural studies by state-of-the-art techniques, relevant to the crystallographic characterization of these materials, in close relationship with their light-absorption properties.

Keywords: methyl ammonium (MA) lead trihalide perovskite, phase transition, octahedral tilting, MA orientation, Fourier synthesis, H location

1. Introduction

Organic-inorganic hybrid perovskites have risen as promising materials for a new generation of solar cells because of their ease of manufacturing and good performance, competing with the best photovoltaic devices based on silicon [1–5]. The introduction of CH₃NH₃PbX₃ (X = Br and I) as the absorber material in an electrolyte-based solar cell structure established the beginning of perovskite-based photovoltaics [2]. However, the power conversion efficiency (PCE) and cell stability were low due to the corrosion of the perovskites by the liquid electrolyte. The replacement of the liquid electrolyte with a solid hole-transporting material led to a key progress in 2012, resulting in both higher PCE and cell stability [3]. Subsequently, great efforts have been devoted to the improvement of these hybrid

perovskite-based cells, including the development of a wide range of architectures, which allowed the PCEs to increase up to 23% within the past years [6]. These halide perovskites have been shown to be finer and to exhibit more suitable optical and electrical properties, like the adaptability of the band gap by introducing different halides (i.e., bromide, chloride, iodide) and its relative proportion in the perovskite [7–9], the high absorption coefficient [10], and the long lifetime of the photogenerated species [11].

$CH_3NH_3PbI_3$-based perovskite solar cells have been more extensively investigated, due to their fast charge extraction rates and their near-complete visible light absorption, related to a relatively low band gap, around 1.6 eV [11, 12]. However, the poor stability of $CH_3NH_3PbI_3$ and rapid degradation in humidity has remained a drawback for its practical application, as a commercialized product [13–16]. $CH_3NH_3PbBr_3$ constitutes a promising alternative, which presents a good charge transport in devices due to its long exciton diffusion length [17]. In addition, its cubic phase and low ionic mobility lead to a better stability under air and moist conditions, compared to the pseudo-cubic $CH_3NH_3PbI_3$ phase, [7, 17–19]. Nevertheless, there are some undesirable features to be concerned about in these bromide-based perovskites; it is the case of a larger band gap (2.2 eV), which decreases the solar light absorption [20, 21], the relatively large exciton binding energy and the reduced light absorption beyond its band edge at 550 nm (linked to its, previously indicated, larger band gap), associated with more limited efficiencies of $CH_3NH_3PbBr_3$ solar cells [7, 18, 19, 22–24].

In parallel with the evaluation of the influence of a particular chemical composition of the perovskite, it is mandatory to determine the crystallographic structure under conditions in which the sample will be used. As other perovskite structures, $CH_3NH_3PbBr_3$ consists of a framework constituted by corner-sharing $PbBr_6$ octahedra, determining large cages where $CH_3NH_3^+$ units are located. In order to correlate the crystal structure of the perovskites with their electro-optical properties, it is necessary to exhaustively study the structural details, including the orientation of the methylammonium (MA) units within the perovskite cage in the course of phase transitions. Although synchrotron XRD data are essential, this can only be fully accomplished using neutrons as a probe due to the presence of protons. Usually, the MA configuration is linked to the rotation or tilting of the PbX_6 octahedra; the more symmetric the octahedral framework is, the more delocalized appears the organic unit inside the inorganic cage. This information is essential to establish relationships between these structures and the macroscopic phenomenology (optical and physical properties when these compounds are used as optoelectronic materials).

$MAPbBr_3$ was previously studied by diffraction techniques in single crystal form by X-ray or in deuterated samples by neutron beams [25–27]. On the other hand, $CH_3NH_3PbCl_3$ is also an alternative material that presents a wider band gap (3.1 eV), being also sensitive to the UV region. Furthermore, this compound exhibits a fast photoresponse and long-term photostability, having a charge carrier concentration, mobility, and diffusion length comparable with the best-developed crystal structures of $CH_3NH_3PbI_3$ and $CH_3NH_3PbBr_3$ [28–30]. However, both $CH_3NH_3PbCl_3$ and the mixed anion $CH_3NH_3Pb(Br_{1-x}Cl_x)_3$ have been less investigated [31].

In this chapter, we review our previous work on the $CH_3NH_3Pb(Br_{1-x}Cl_x)_3$ system, where we have investigated the crystallographic features in powdered, non-deuterated samples, using the mentioned state of the art techniques, neutron and synchrotron X-ray diffraction [32–34]. The crystal structure of $MAPbBr_3$ has been determined and refined at different temperatures, describing the evolution of the orientation of MA group in the 120–295 K temperature range. We found a partial delocalization in the cubic phase (at room temperature), where C and N atoms present large multiplicity positions, becoming progressively localized across the sequence cubic-tetragonal

and finally orthorhombic, at 120 K, with MA units fully oriented in the (101) plane [32]. Regarding to Cl-containing phases, a systematic study of the structural properties of hybrid mixed perovskites $CH_3NH_3Pb(Br_{1-x}Cl_x)_3$ by combining synchrotron X-ray diffraction and UV-vis spectroscopic analyses reveals that the band gap can be chemically tuned according to the Br/Cl ratio. The orientation of the organic MA units may also play an important role in the optoelectronic properties of these materials. By neutron powder diffraction, we found at RT three different orientations depending on the chlorine content and, therefore, on the unit-cell size. At lower temperatures, we unveiled that the halide disorder prevents the cooperative rearrangements needed to drive the octahedral PbX_6 tiltings in intermediate Br/Cl ratios; only $CH_3NH_3PbCl_3$ underwent conspicuous phase transitions (cubic at room temperature, evolving to tetragonal and orthorhombic at 120 K) [33]. H-bond interactions with the halide ions stabilize these conformations, in accordance to reported theoretical calculations [34].

2. Crystal growth

The crystal growth of $CH_3NH_3Pb(Br_{1-x}Cl_x)_3$ (x = 0, 0.33, 0.5, 0.67 and 1) [32–34] was made from stoichiometric amounts of CH_3NH_3X and PbX_2 (X = Cl, Br). Previously, the methyl ammonium bromide and methyl ammonium chloride were synthesized from methyl amine (CH_3NH_2) and the corresponding acid HBr and HCl, respectively, according to the following reaction:

$$CH_3NH_2 + HX \rightarrow CH_3NH_3X \text{ (from X = Br to Cl)} \tag{1}$$
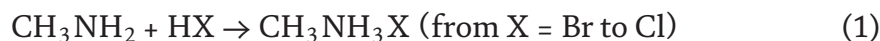
Then, the obtained methyl ammonium halides were reacted with the lead halide in stoichiometric amounts in dimethyl formamide (DMF) according to the following reaction:

$$CH_3NH_3X + PbX_2 \rightarrow CH_3NH_3PbX_3 \text{ (from X = Br to Cl)} \tag{2}$$

From this procedure, the mixed halide perovskites were obtained as well crystallized materials, showing crystals of variable sizes and colors, varying from orange for $CH_3NH_3PbBr_3$ to white for $CH_3NH_3PbCl_3$, adopting progressively paler hues of yellow as Cl content increases, as shown in the optical microscope images included in **Figure 1**. The effect of halide composition on the morphology and structure of
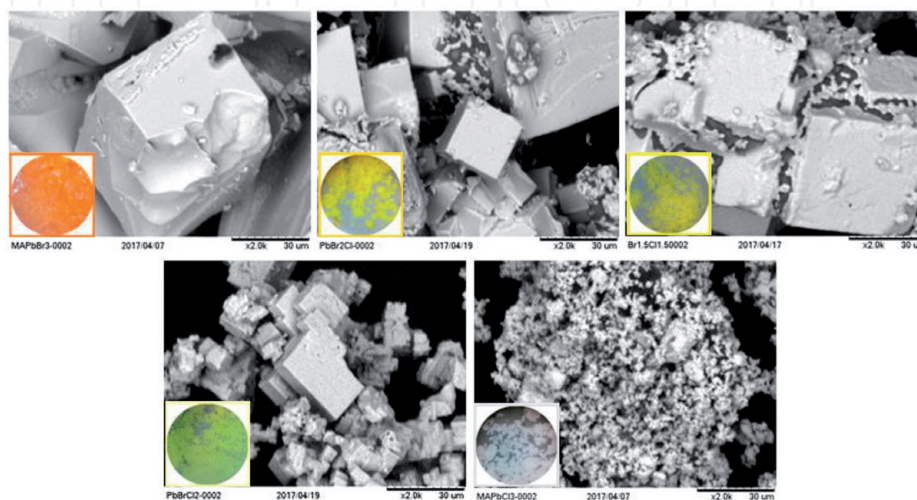

Figure 1.
SEM images of the mixed perovskites and optical microscope images of as-grown $CH_3NH_3PbX_3$ (from X = Br to Cl) perovskites. The insets show the color variation as Cl is introduced.

crystals was observed in SEM images as is also shown in **Figure 1**. In all cases, the obtained perovskites show cuboid-type microcrystals. The content of chloride induces a decrease in the size of the crystals of the mixed perovskites.

3. Synchrotron X-ray diffraction studies

Synchrotron X-ray diffraction (SXRD) technique provides an extreme angular resolution of the patterns, useful to define the symmetry of the different phases and to determine its evolution below room temperature (RT). The crystal structures at RT are cubic, and they are well defined in the space group $Pm\bar{3}m$. In this model, the lead and bromine atoms are placed in $1a$ (0,0,0) and $3d$ (1/2,0,0) Wyckoff sites, respectively; and the organic unit is positioned in $1b$ (1/2,1/2,1/2). **Figure 2a** shows selected reflections of the Rietveld refinements corresponding to x = 0 in comparison with x = 0.33, 0.5, 0.67, and 1 members at RT. **Figure 2b** and **c** plot the unit-cell parameter variation and the anisotropic atomic displacement parameters (ADPs) of X site, respectively. The unit-cell parameters exhibit an expected reduction as the amount of Cl increases, but this change is not linear. As shown in the **Figure 2c**, the disks perpendicular to the Pb–X–Pb bonds exhibit an oblate shape, meaning the ADPs of X atoms are considerably anisotropic. Since the thermal vibrations in this direction are allowed in perovskites, this behavior is not surprising. However, for the intermediate mixed halide phases (x = 0.33, 0.5, and 0.67), the ADPs show a non-monotonic variation compared to both end members (x = 0 and 1), although the difference does not overcome two times the standard deviations and is less significant.

These anomalies were assigned to the structural disorder introduced by the mixture of halides, for x = 0.33, 0.5, and 0.67. The ADPs should account for the structural
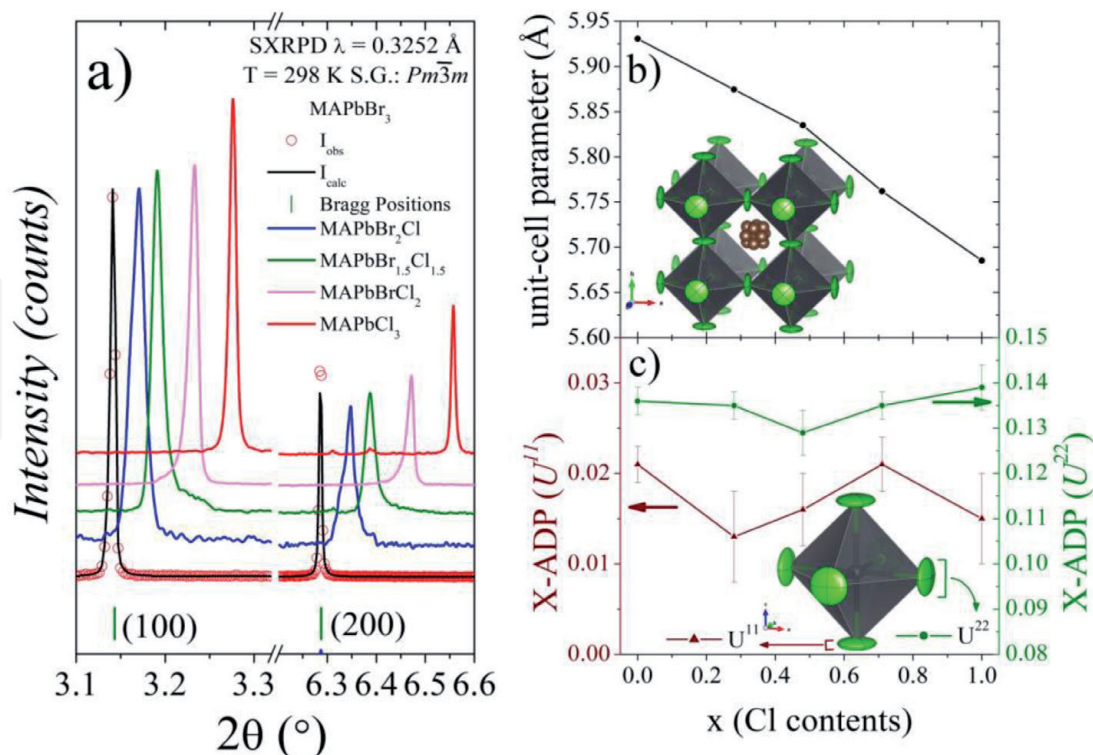

Figure 2.
(a) SXRD profiles for CH₃NH₃PbBr₃ at RT, after a pattern matching showing the characteristic perovskite peaks and the absence of impurities. Red circles are the experimental points, the black full line is the calculated profile. The green vertical marks represent the allowed Bragg positions in the Pm ⁻ 3m space group. The Cl-doped patterns are added in this plot to compare with the bromide parent. (b) Unit-cell parameters evolution and (c) variation of the anisotropic atomic displacement parameters (ADP) of X site with the Cl contents.
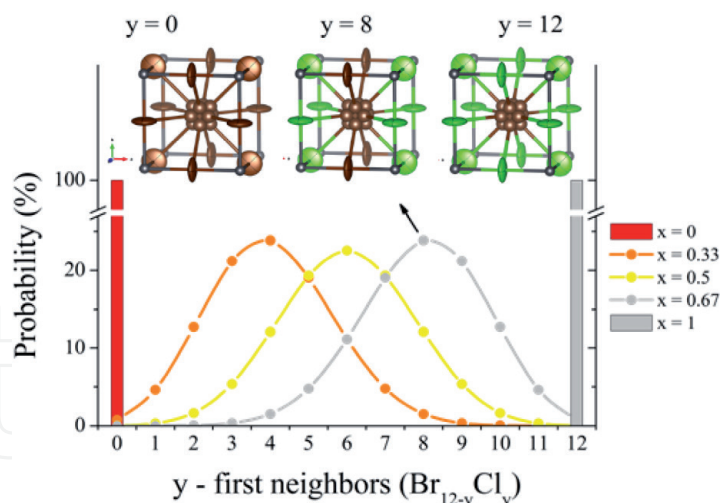
Figure 3.
Statistical probability distribution of the halide environment in $CH_3NH_3Pb(Cl_{1-x}Br_x)_3$ (x = 0, 0.33, 0.5, 0.67, and 1).

disorder, which can also generate a perturbation in the interactions between the inorganic PbX_6 skeleton and the methyl-ammonium units. This perturbation is absent in MAPbBr₃ and MAPbCl₃, containing single halide ions. In **Figure 3**, a statistical probability distribution of the halide environment of MA groups is plotted, showing this behavior for the different samples ($CH_3NH_3Pb(Cl_{1-x}Br_x)_3$, x = 0, 0.33, 0.5, 0.67, and 1). It is remarkable that for MAPbBr₃ and MAPbCl₃ the probability is 100%, because all of their MA units are coordinated to 12 Br or Cl atoms; this state contrasts with the mixed halide situations (x = 0.33, 0.5, and 0.67). These distributions reveal the high structural disorder given in mixed situations, in contrast to both end members. These probably induce tensions in the lattice preventing a linear behavior between the pure bromine and chlorine compounds. The inserts in **Figure 3** include illustrative schemes of the extreme situations in comparison with an intermediate case where the MA is coordinated to eight chlorides and four bromides, y = 8.

The thermal variation of the crystallographic structures was followed between 120 K and RT. **Figure 4** shows the temperature evolution of selected diffraction
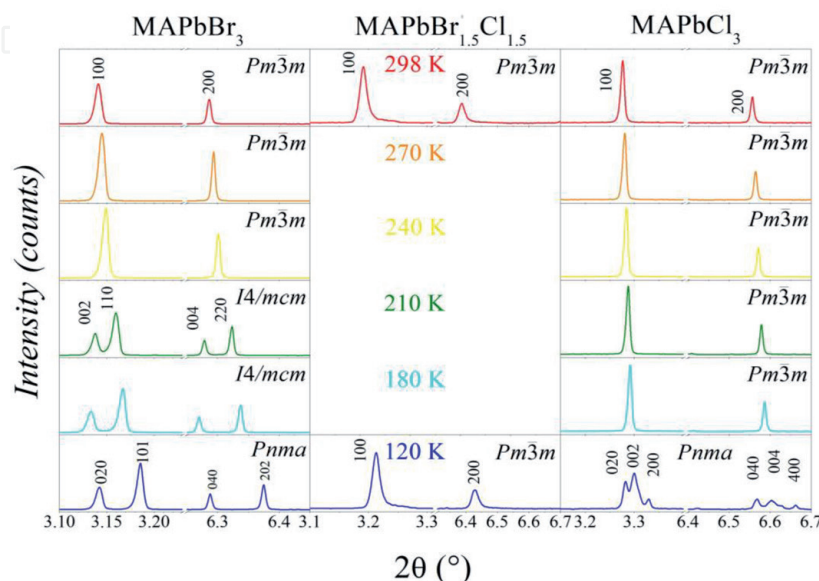

Figure 4.
Thermal evolution of selected diffraction lines in which the phase transitions are evidenced, from SXRD data, collected at MSPD diffractometer at ALBA synchrotron (Spain) [32–34].

lines for all members of the series. In this temperature range, only both end members of the series (x = 0 and 1) exhibit phase transitions; in contrast, for the mixed halide compositions, no phase transitions have been detected, observing cubic structures ($Pm\bar{3}m$) either at RT or down to 120 K, as illustrated in **Figure 4**.

Previous works also report on the polymorphic evolution of Br and Cl phases. Swainson et al. report on two phase transitions for MAPbBr$_3$: $Pnma$ $\leftarrow$ ($\approx$150 K) $\rightarrow$ $I4/mcm$ $\leftarrow$ ($\approx$223 K) $\rightarrow$ $Pm\bar{3}m$ [25]. These phases were also described by other authors from single crystal data [26, 27]. It was reported by Poglitsch et al. that the MAPbCl$_3$ perovskite goes through two phase transitions: $P222_1$ $\leftarrow$ (173 K) $\rightarrow$ $P4/mmm$ $\leftarrow$ (179 K) $\rightarrow$ $Pm\bar{3}m$ [35]. Afterward, Chi et al. stated that the orthorhombic polymorph corresponds to the $Pnma$ space group, but with a unit-cell twice the size of the cubic aristotype (a $\approx$ b $\approx$ c $\approx$ 2a$_p$) [36].

Our work on CH$_3$NH$_3$PbBr$_3$ shows that the SXRD patterns collected at RT, 270 and 240 K correspond to cubic symmetry, defined in the $Pm\bar{3}m$ space group; at 210 and 180 K to tetragonal symmetry in the $I4/mcm$ space group; and at 120 K to orthorhombic symmetry, defined in the $Pnma$ space group [32]. On the other hand, CH$_3$NH$_3$PbCl$_3$ remains stable as cubic down to 180 K; however, the SXRD patterns at 120 and 150 K exhibit a conspicuous splitting of some reflections [33]. According to the model proposed by Chi et al. [36]; this splitting (at 120 and 150 K) is possible. Nevertheless, some extra lines during the preliminary refinements seem to indicate that there is another phase, orthorhombic ($Pnma$), resembling the one observed in MAPbBr$_3$ ($a \approx \sqrt{2}a_p$; $b \approx 2a_p$; $c \approx \sqrt{2}a_p$). If the coexistence of both phases mentioned is taken into consideration, a satisfactory refinement at 150 and 120 K can be completed, with only slight differences in the peak width; being wider for the case of the conventional $Pnma$ phase compared to the doubled $Pnma$ structure. A possible explanation could be that microstructural features cause this phase mixture.

For MAPbCl$_3$, the mechanism or transient state from cubic to orthorhombic symmetry has been until now only partially known. As indicated previously, the tetragonal phase ($P4/mmm$) was observed in a very narrow range of temperature, 172.9–178.8 K. Up to now, no new reports have appeared on this transient tetragonal phase. Several patterns were collected sequentially [33] in this narrow temperature range, with intervals of 2.5 K, as illustrated in **Figure 5a**, where a different phase is evidenced between 169 and 164 K. This phase, corresponding to the pattern at 167.2 K, was initially fitted to the tetragonal model; however, additional diffraction lines were observed evidencing an orthorhombic symmetry. Matching the patterns observed at 120, 150, and 160 K, $Pnma$ ($a \approx \sqrt{2}a_p$; $b \approx 2a_p$; $c \approx \sqrt{2}a_p$) provided a satisfactory fit at 167.2 K. In this last case, at low temperatures the unit-cell
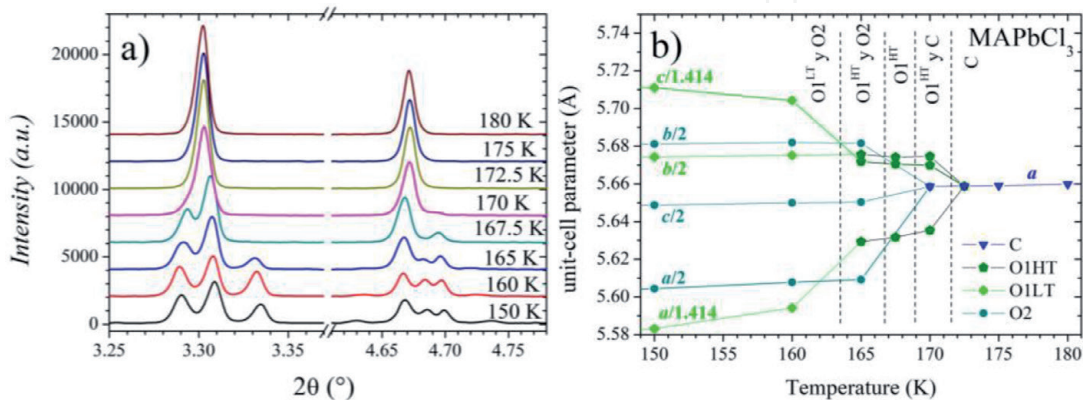

Figure 5.
(a) Selected angular region of the SXRD patterns of MAPbCl$_3$ at increasing temperatures (from 150 to 180 K), illustrating the evolution and splitting of some characteristic reflections. (b) Thermal evolution of the unit-cell parameters of the MAPbCl$_3$ perovskite in the same temperature range [33].
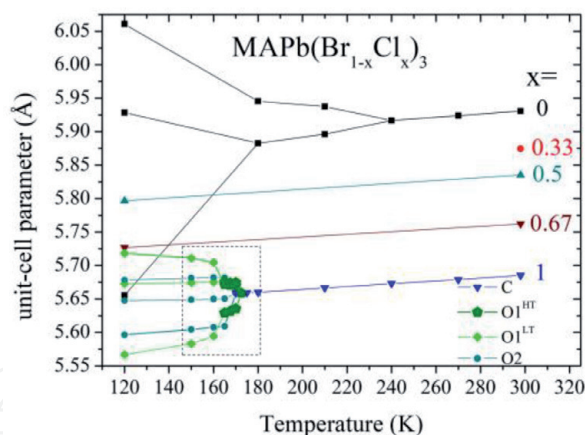
Figure 6.
Thermal evolution of the unit-cell parameters of MAPb$(Br_{1-x}Cl_x)_3$ perovskites in the 120–300 K temperature range [33].

parameters tend to be considerably less split. In **Figure 5b**, the unit-cell parameters variation as a function of temperature is displayed in this narrow temperature range.

From these facts, it is clear that MAPbCl₃ goes through a more complex transition compared to the ones already reported. To summarize, there are three phases: cubic, orthorhombic ($a \approx \sqrt{2}a_p$; $b \approx 2a_p$; $c \approx \sqrt{2}a_p$), and a second orthorhombic ($a \approx 2a_p$; $b \approx 2a_p$; $c \approx 2a_p$), as indicated in **Figure 5b** as C, O1, and O2, respectively. Moreover, the O1 phase can be separated into two states with different distorted degrees: $O1^{HT}$ and $O1^{LT}$. In the first case, the unit-cell parameters splitting with respect to cubic a_p is substantially lower than in the second case. Moreover, an inversion between $b/2$ and $c/\sqrt{2}$ values is observed in **Figure 5b**. Additionally, a high tetragonality is observed in $O1^{HT}$ where the following relationship between the unit-cell parameters is observed: $a/\sqrt{2} < b/2 \approx c/\sqrt{2}$. This fact can explain the previous description in the tetragonal symmetry in this short temperature range.

As reported in [32, 33], MAPbCl₃ and MAPbBr₃ are stable above 179 and 237 K respectively; therefore, it is relevant to mention the lack of any other phase transition down to 120 K in mixed halide perovskites. The anion disorder in the mixed-halide phases could explain this surprising behavior. As it was previously mentioned, the interactions between the organic and inorganic parts differ from one sample to another within the present series (see **Figure 3**). The phase transitions are prevented due to the halide disorder, because it does not allow the rearrangements that are required in terms of octahedral tilting. Finally, SXRD measurements and their analysis (Rietveld refinements) provide new evidence that allows to complete the polymorphic evolution in the MAPb$(Br_{1-x}Cl_x)_3$ family, as displayed in **Figure 6**.

4. Neutron diffraction studies

The neutron powder diffraction (NPD) investigation is essential to obtain a detailed description of these hybrid materials. The NPD data were collected at the D2B diffractometer (ILL, France) [32, 34]. In particular, the distribution of MA groups can be elucidated taking advantage of the high contrast in the coherent scattering lengths of Pb, Br, Cl, C, N, and H, of 9.405, 6.795, 9.577, 6.646, 9.36, and −3.739 fm, respectively.

However, there is an issue in the resolution of the structure that needs to be considered. The incoherent background in a powder experiment is considerably large due to the presence of hydrogen, which has an important inelastic component

(25,274 barns) that gives rise to a significant incoherent background. This is not an obstacle for the crystallographic Rietveld refinement if sufficient statistic is achieved during the measurement.

On the other hand, due to the negative contribution of hydrogen to the scattering, some strategies are necessary to find the adequate distribution of MA in the inorganic PbX_6 framework. First, the instrumental and the unit-cell parameters were refined using the Le Bail method. The structure of the octahedral PbX_6 framework was eventually considered in the model, placing the lead atoms at 1a (0,0,0) sites and bromine/chlorine atoms at 3d (1/2,0,0) positions in the $Pm\bar{3}m$ space group. Later on, Difference Fourier Maps (DFM) were acquired from the observed and calculated patterns, unveiling the missing negative and positive nuclear density (in scattering length) around A site of the perovskite structure (1b (1/2,1/2,1/2)).

This analysis in $MAPbBr_3$ [32] yields the positive (represented in yellow) and negative (represented in blue) isosurfaces shown in **Figure** 7a, which correspond to the C/N and H positions, respectively. The negative scattering regions are due to the negative scattering of protons while the positive zone corresponds to C/N atoms. These nuclear densities support that the MA units are delocalized in the A site of the perovskite. Considering the positive density, the C/N atoms are located at 24i (1/2,y,y) positions. Then, the H positions can be elucidated from the geometric shape of methylammonium group. The observed geometry can be satisfied with two hydrogen atoms located at 24 l (1/2,y,z) and 24 m (x,x,z) Wyckoff sites. This analysis in $MAPbBr_3$ reveals that the MA group is delocalized at room temperature along the [110] direction, involving six possible orientations.

In contrast, the DFM for $MAPbBr_2Cl$ show that the positive and negative densities match exactly with those expected for the MA cations oriented along [111] directions. It is possible to deduce that the C/N and H atoms are placed at 8 g (x, x, x) and 24 m (x, x, z) Wyckoff positions, respectively (**Figure** 7b). $MAPbBr_{1.5}Cl_{1.5}$ exhibits a peculiar negative distribution (see **Figure** 7c), where there are four negative zones along the [001] directions, suggesting that the MA units are along this direction. However, along [111] directions, there also appears a non-negligible density, which is unrealistic. This dichotomy is resolved by analyzing the C/N density from the positive surface; it unveils that the C/N atoms are indeed delocalized along the [100]
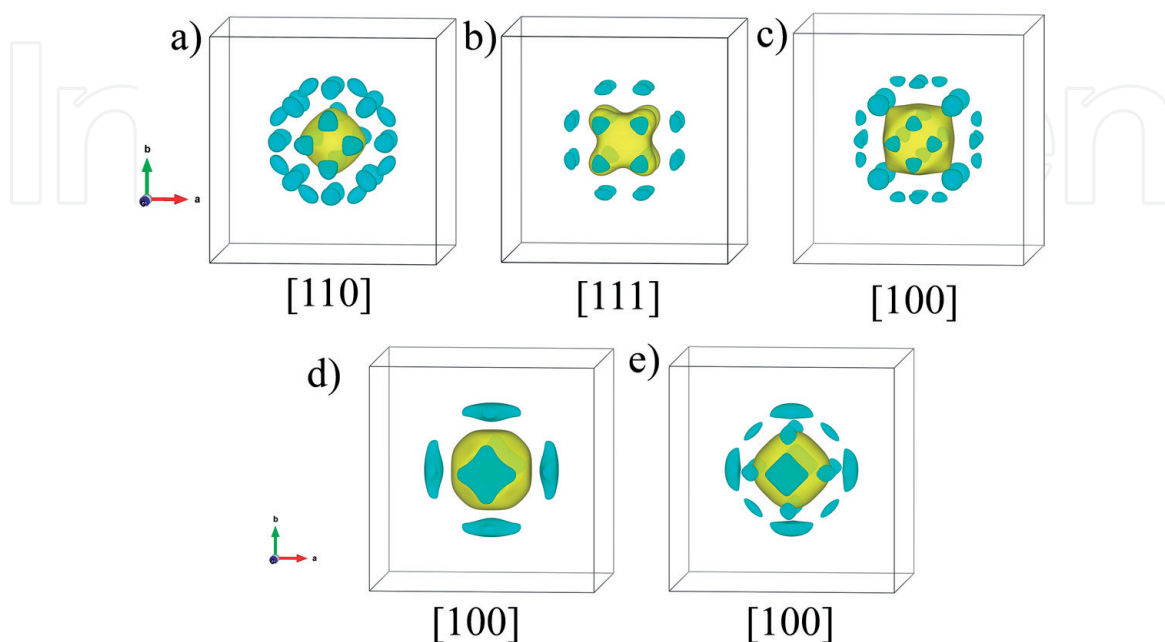

Figure 7.
DFM isosurfaces of $MAPb(Br_{1-x}Cl_x)_3$ series for x = 0 (a), 0.33 (b), 0.5 (c), 0.67 (d), and 1 (e), from NPD data [32, 34].

directions. The same procedure in MAPbBrCl$_2$ and MAPbCl$_3$, see **Figure 7d** and **e**, shows that the MA groups are oriented along [100] directions, in the same way as MAPbBr$_{1.5}$Cl$_{1.5}$. From this result, which only can be obtained from NPD data, a clear restriction in the MA delocalization is unveiled, evolving from [110] to [111] and finally to [100] directions, while X is progressively enriched in Cl⁻ anions.

From the Fourier synthesis maps, a crystallographic model can be built with the MA configurations, to start the structural Rietveld refinements from the NPD data. Additionally, the MA displacement toward –NH$_3$ group also can be considered, as it was proposed from theoretical calculations [37, 38]. This last approach corresponds to the plausible chemical interactions between the organic cation and inorganic framework; the greater electronegativity of nitrogen produces H-bond interactions shorter than C–H···X. Considering this last fact and the DFM results, the Rietveld refinement of NPD data was made. Minor amounts of MACl were identified and included in the refinements as second phase in the chlorine phase. The Rietveld fits for MAPbBr$_3$ and MAPbCl$_3$ are illustrated in **Figure 8**. The crystal structure data after these refinements are listed in **Table 1** for all the compositions. This table shows the three different combinations of C/N and H positions considering three possibilities for the MA delocalization in the PbX$_6$ framework observed in the MAPb(Br$_{1-x}$Cl$_x$)$_3$ series. The variation of the unit-cell parameter with the Cl-doping is illustrated in **Figure 9**; here, a change of slope is observed in the perovskite with an equimolar amount of Br and Cl atoms, according to the anomaly obtained from synchrotron data.

For x = 0.5, 0.67, and 1, the unit cell experiences a contraction, keeping a constant slope as Cl is introduced, with the MA oriented in the same direction. On the other hand, for x = 0 and 0.33, the unit cell parameters do not follow this trend, the MA orientation is different.

A feature to highlight is the difference in negative density (arising from H positions) observed between [111] and [100] orientations. While along the [111] direction, the three terminal H atoms of the H$_3$C-NH$_3^+$ units are fixed, as it is shown in **Figure 7b**. From the negative density displayed in **Figure 7c–e**, it is noticeable that four H atoms are comprised in the (100) plane, suggesting that the MA units occupy equivalent positions, so that each H points to each of the four halides in the edges of the perovskite unit cell, thus manifesting the importance of H···X hydrogen bonds. This bonded H is located in H11 site and the other two H of the amine group are located in the H12 site. Similarly, the methyl group is formed by C2, H21, and H22 atoms.
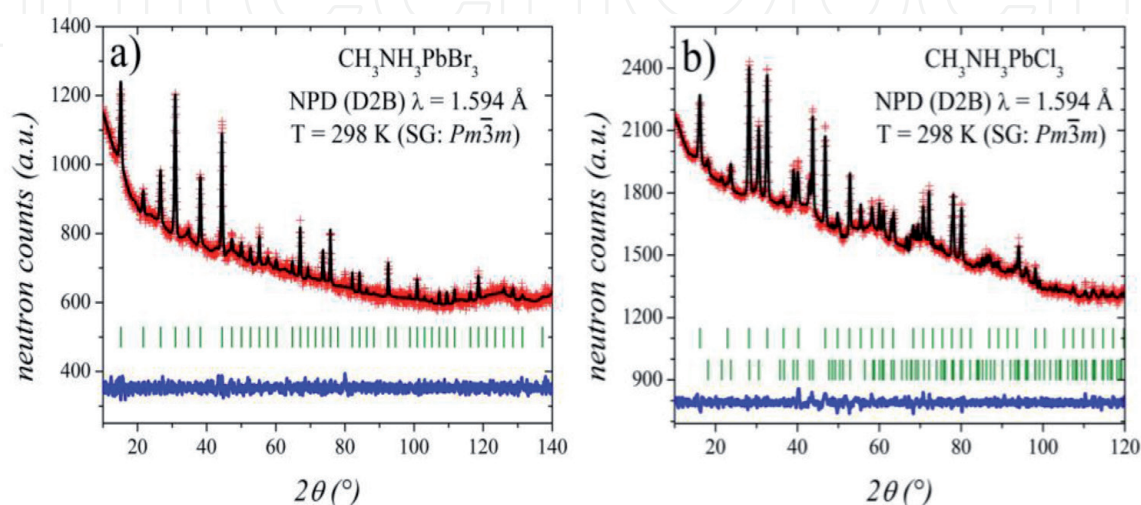

Figure 8.
Rietveld plots of a) MAPbBr$_3$ and b) PbPbCl$_3$ from NPD data, at RT.

MAPb(Br$_{1-x}$Cl$_x$)$_3$	x = 0 [32]	x = 0.33 [34]	x = 0.5 [34]	x = 0.67 [34]	x = 1 [34]
a (Å)	5.9259(4)	5.8454(8)	5.80459(6)	5.76955(7)	5.6813(5)
Pb (1a) (0,0,0)					
$U^{11} = U^{22} = U^{33}$	0.025(2)	0.048(3)	0.0313(3)	0.031(2)	0.0239(4)
Br$_{1-x}$Cl$_x$ (3d) (0.5,0,0)					
x	0	0.38(3)	0.55(5)	0.67(8)	1
U^{11}	0.018(5)	0.028(5)	0.0147(5)	0.026(4)	0.0471(8)
$U^{22} = U^{33}$	0.138(5)	0.130(5)	0.1318(6)	0.104(4)	0.1151(7)
N/C	C/N (0.5,y,y) 0.407(2)	N1(x,x,x) 0.5809(5)	N1(0.5,0.5,z) 0.6290(4)	N1(0.5,0.5,z) 0.6294(5)	N1(0.5,0.5,z) 0.6594(5)
		C2(x,x,x) 0.4378(5)	C2(0.5,0.5,z) 0.3777(6)	C2(0.5,0.5,z) 0.3782(6)	C2(0.5,0.5,z) 0.4113(5)
U$_{iso}$*/U$_{eq}$	0.039(7)	0.061(1)*	0.051*	0.051*	0.039(1)*
H	H1(0.5,y,x) 0.414(9) 0.247(9)	H11(x,y,x) 0.5839(6) 0.7363(9)	H11(0.5,y,z) 0.664(1) 0.702(3)	H11(0.5,y,z) 0.665(1) 0.702(3)	H11(0.5,y,z) 0.670(1) 0.720(2)
	H2(x,x,z) 0.326(3) 0.448(4)	H12(x,y,x) 0.4416(7) 0.2841(8)	H12(x,y,z) 0.640(1) 0.419(1) 0.702(3)	H12(x,y,z) 0.641(1) 0.418(1) 0.702(3)	H12(x,y,z) 0.6445(9) 0.4166(9) 0.720(2)
			H21(0.5,y,z) 0.331(1) 0.305(3)	H21(0.5,y,z) 0.331(1) 0.306(1)	H21(0.5,y,z) 0.326(1) 0.351(2)
			H22(x,y,z) 0.357(1) 0.583(1) 0.305(3)	H22(x,y,z) 0.356(1) 0.583(1) 0.306(3)	H22(x,y,z) 0.354(1) 0.585(1) 0.351(2)
U$_{iso}$*/U$_{eq}$	0.06(1)	0.063*	0.063*	0.063*	0.059(2)*
R$_p$(%)	1.3	1.3	1.0	1.2	0.8
R$_{wp}$(%)	1.6	1.7	1.3	1.5	0.9
χ^2	1.1	1.1	1.3	1.1	1.2
R$_{Bragg}$(%)	3.9	10.8	6.5	6.5	6.4

Table 1.
Crystallographic data for MAPb(Br$_{1-x}$Cl$_x$)$_3$ with x = 0, 0.33, 0.5, 0.67, and 1 at room temperature from NPD.

Looking back at the unit-cell variation, the contraction of the PbX$_6$ octahedron as Cl is introduced leads to a localization of the MA units, limiting their orientation. This decrease has been deeply studied below room temperature, as the crystal goes through the phase transitions: cubic-tetragonal-orthorhombic [37, 39, 40]; however, in this case, CH$_3$NH$_3$Pb(Br$_{1-x}$Cl$_x$)$_3$, the behavior is observed in the same crystal system at RT [34]. This finding shows that the MA freedom degree reduction can occur either by a decrease in the symmetry or by size reduction (keeping the symmetry) in the PbX$_6$ network. These discoveries renew the question whether the inorganic framework deformation occurs and then the MA units accommodate in the preferred directions, or the reduction in the MA freedom degree enables the
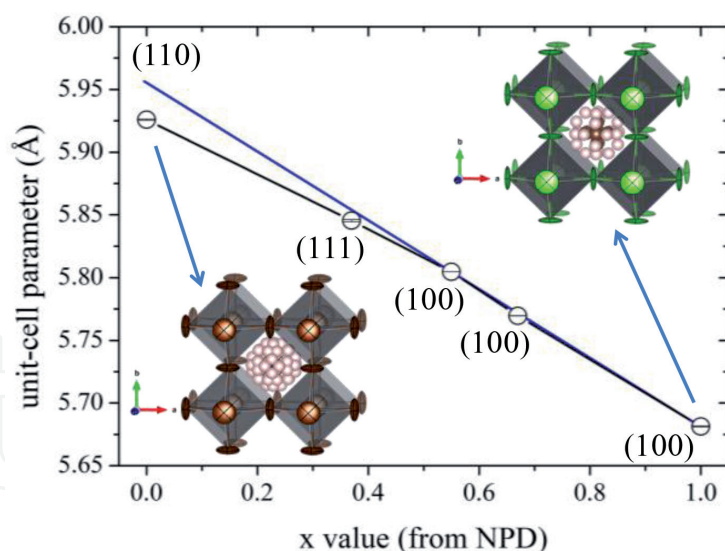
Figure 9.
Unit-cell parameters variation for $MAPb(Br_{1-x}Cl_x)_3$ from NPD data, at RT.

inorganic framework to adopt a low symmetry. This dichotomy is as the *chicken and egg* paradox, which has previously been analyzed from DFT calculations, concluding that phase transitions occur as a synergic effect between both organic and inorganic components [38]. In the present case, the MA restrictions occur without symmetry reduction in the inorganic framework, but as a consequence of a contraction in the unit-cell size, so it is possible to think that the PbX_6 lattice drives the MA freedom degree. However, it is only an appreciation and it is not enough to resolve this dichotomy.

On the other hand, the role of H···X interactions in the MA conformations is not unknown [41, 42] but shows some controversy among the different results. Theoretical studies from DFT indicate that the energy difference between the low index [100], [110], and [111] orientations of the MA units is similar, but with a subtle preference for the [100] orientation in the tetragonal $MAPbI_3$ [40]. However, the ab initio simulations performed by Shimamura et al. [43] unveiled that [110] was the preferred orientation due to the H···X interactions in $MAPbI_3$. Differently, Li et al. identify [111] and [100] for the $MAPbI_3$ and $MAPbCl_3$ perovskites as the favorable orientations [38]. Afterward, Varadwaj et al. reinforced this last idea by also stating that these orientations were the most energetically favorable [37]. Although there is significant theoretical work regarding the MA units orientation in cubic symmetry, experimental evidence is lacking [25, 27, 36]. It is the case of the Baikie et al. [27] report that focuses on the three structures for X = I, Br, and Cl from X-ray and neutron diffraction data. In all the cases, the MA components were refined in the [110] direction. In this context of theoretical results, the considerations made in the $CH_3NH_3Pb(Br_{1-x}Cl_x)_3$ refinements offer new possibilities to achieve a detailed analysis of the crystal studies in comparison with these theoretical works. Once the atomic positions are refined, a "deconvolution" of the MA units orientation can be done for the directions [111] and [100]. The H···X interactions obtained can be compared with those predicted theoretically.

The MA units within the cubic unit cell are presented in **Figure 10**, the three alignment possibilities ([110], [111], and [100]) are shown. The MA in $MAPbBr_3$ is aligned along [110] and, as can be seen in **Figure 10a** and **d**, in this orientation the N–H bonds point toward face centers or cube corners forming smalls angles N–H···Br; hence, this configuration is not suitable for hydrogen bonding. On the other hand, for x = 0.33 (along [111] direction), the H–C and H–N interact with a

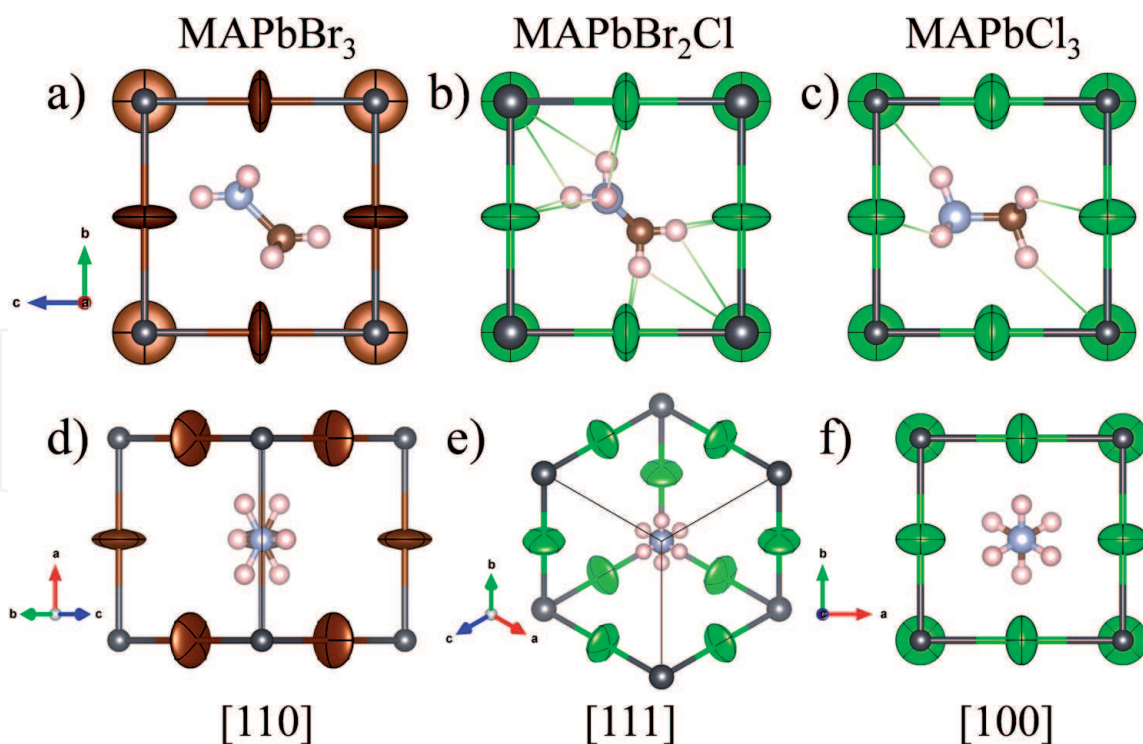**Figure 10.**
Methyl-ammonium conformations in the MAPbBr3 (a) and (d), MAPbBr2Cl (b) and (e) and MAPbCl3 (c) and (f) perovskites, from NPD data at RT. The lowest figures (d), (e) and (f) are shown along the MA direction.

unique halide (X = $Cl_{0.33}Br_{0.67}$) with a distance of 2.921(5) and 3.088(5) Å, respectively (**Figure 10b** and **e**). As mentioned, the MA conformation is slightly displaced, the (C)H···X distances are larger than (N)H···X, which could be explained by the bigger electronegativity of N compared to C.

Varadwaj et al. reported on DFT calculations for the $MAPbBr_3$ perovskite [37]; the distances were determined, being ≈2.44 and ≈3.47 Å for (N)H···X and (C) H···X, respectively, in agreement with the NPD experimental results. Carrying out the same procedure for x = 0.5, 0.67 and 1, we can determine the orientation of the MA units, which resulted to be [100]. The MA units can be rotated in four positions along the three [100] directions giving 12 possible conformations. With the help of DFT calculations, the orientation of the MA unit for bromine and chlorine phases can be estimated, with the additional fact that the (N)H···X distances are shorter that the (C)H···X ones [37, 38]. **Figure 10c** and **f** illustrate a MA unit from the obtained C, N, and H atomic positions for $MAPbCl_3$; two different types of H-bonds can be distinguished: normal (N1–H11···X) and bifurcated (N1–H12···X). Similarly, the methyl group shows the same interactions through H21 and H22 atoms. The obtained distances for x= 1 phase are 2.459(8) and 2.615(8) Å for N1–H11···X and N1–H12···X, respectively [38].

The structural refinement from NPD data provide, for the first time, experimental evidence of the MA alignments, confirming the theoretical results reported up to now.

5. Optoelectronic properties

The optoelectronic properties are characterized using different techniques such as diffuse reflectance UV-vis spectra and building a photodetector device where the current-voltage (IV) curves are measured under illuminations. This device was fabricated by drop-casting the perovskite solution onto Au/Cr pre-patterned electrodes.
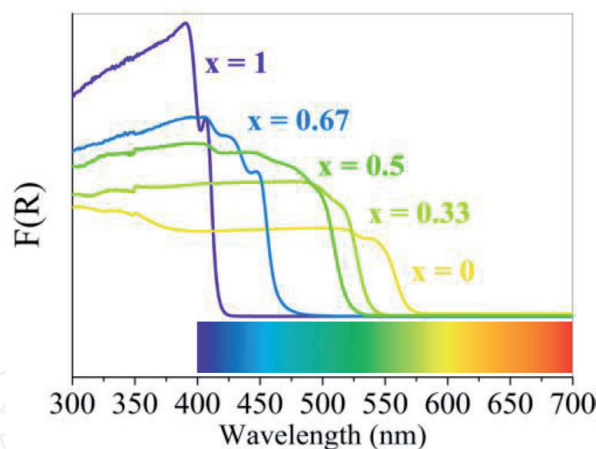
Figure 11.
UV-vis absorption spectra for MAPb(Br₁₋ₓClₓ)₃. The colored line corresponds to the band gap energy.

The UV-vis spectra, illustrated in **Figure 11**, are used to calculate the optical absorption coefficient (α) according to the Kubelka-Munk equation:

$$F(R) = \alpha = (1 - R)2/(2R) \tag{3}$$

where R is the reflectance (%). The optical band gap is determined from the extrapolation of the linear part of the transformed Kubelka-Munk spectrum with the hν axis. Absorbance vs. wavelength of the incident radiation for MAPb(Br₁₋ₓClₓ)₃ series is illustrated in **Figure 11**. In this plot, the included color chart allows accounting for the sample color shown in **Figure 1**.

The absorption edge presents a gradual evolution, which is consistent with the continuous structural changes, mainly with the unit-cell parameter evolution. The energy of the gap experiences an increment as Br is progressively replaced with Cl. This is, in principle, expected as a consequence of the smaller covalency of the lead-halide bonds within the PbX₆ (X = Cl, Br) octahedra [31]. Recent studies by density functional theory (DFT) show that the edges of the valence band and conduction band of CH₃NH₃X₃ perovskites are principally made up of p_X and p_{Pb} states, respectively [44]. It is shown that near the gap, the predominant contribution is brought about by Pb-Pb transitions, involving s-type orbitals. The characteristic absorption band above 3 eV is fundamentally driven by s_{Pb}-p_{Pb} interactions, tuned by the unit-cell
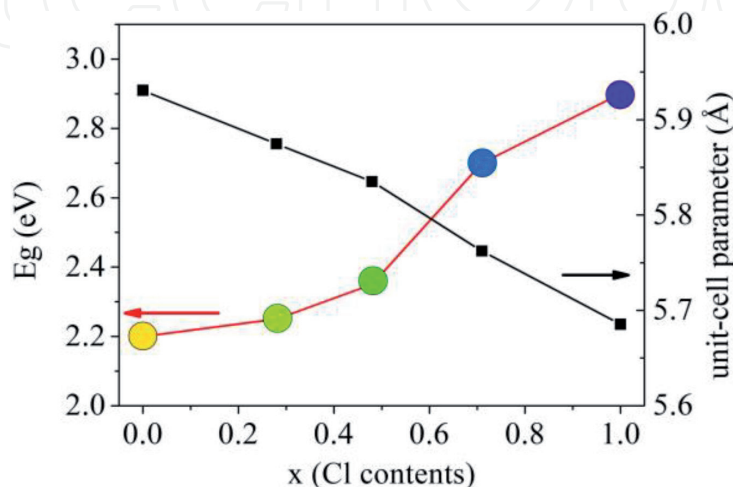

Figure 12.
Comparison between the band gap energy and unit-cell parameter in MAPb(Br₁₋ₓClₓ)₃, as a function of the Cl content, x. The color in the circles corresponds to the band gap energy.

size, with a lower contribution by p_{Pb}-p_X and s_X-p_X transitions. These latter contributions decrease from iodine to bromine and then to chlorine, that is, when increasing the electronegativity of the halide, which accounts for the variation of the gap with the chemical nature of X, as shown in **Figures 11** and **12**. Endres et al. [45] found a remarkably low DOS at the valence band of MAPbX$_3$, from either ultraviolet and inverse photoemission spectroscopies or from theoretical densities of states (DOS), calculated via density functional theory. They found a strong band dispersion at the valence band due to the coupling between halide p and Pb s antibonding orbitals, observing the absence of significant densities of states tailing into the perovskite gaps.

As already mentioned, an interesting feature is that the compositional evolution of the band gap energy (Eg) does not possesses a linear behavior; it seems that the deviation from linearity is reminiscent of that unveiled for the variation of the unit-cell parameters at RT (see **Figure 12**). By additionally contrasting the Eg value with the Pb–X bond lengths, a non-linear behavior is apparent, suggesting that the evolution of Eg is not only related to the inorganic features. From this point of view, it is interesting to consider that, although all these studies are based on the nominally simple cubic perovskite structure, these compounds are in fact very complex. For example, in (CH$_3$NH$_3$)PbI$_3$, the dynamics associated with the (CH$_3$NH$_3$)$^+$ ions are still not fully understood, although ab initio calculations show [46] that at room and higher temperature, the rotation of CH$_3$NH$_3$ molecules can be viewed as effectively giving local structures that are cubic- and tetragonal-like from the point of view of the PbI$_3$ framework, though in fact having lower symmetry. These arrangements are locally polar, with sizable
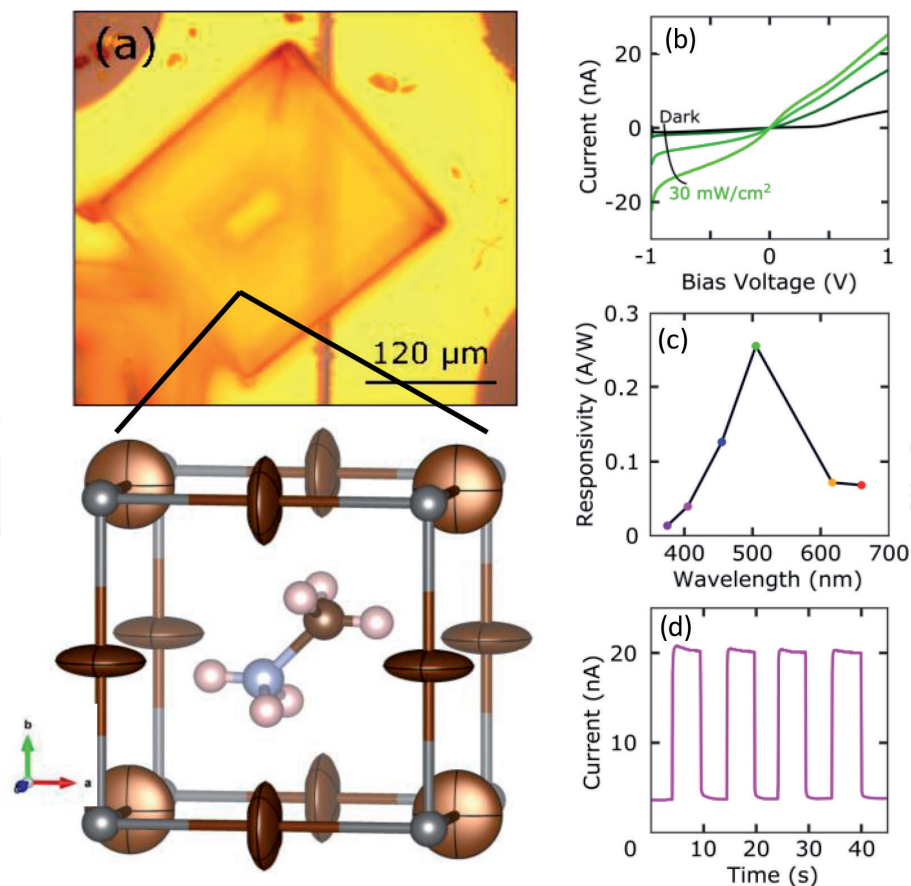

Figure 13.
(a) View of the photodetector device, including a crystal of MAPbBr$_3$ grown between two pre-patterned electrodes, separated apart by 10 μm. (b) Current-voltage (I-V) curves obtained with 505-nm illumination, by changing the incident optical power densities. (c) Spectrum displaying the responsivity for different wavelengths. (d) Generated photocurrent vs. time, when a modulated illumination is applied with a fixed voltage [32].

polarization, ~10 μC/cm^2 due to the dipoles on the organic part [46]. The structural transitions are thus analogous to the transitions between two ferroelectric structures, where there is strong screening of charged defects that can lead to enhanced mobility and charge collection.

This observation seems to confirm that the increase in the Eg with the amount of Cl$^-$ is closely correlated with the effect of the MA and its freedom degree in the inorganic framework. The change in the MA delocalization upon the incorporation of smaller Cl$^-$ anions is an additional parameter to be considered in the tuning of the optical properties of these hybrid materials.

Furthermore, the potential of these materials in optoelectronic applications can be exemplified for MAPbBr$_3$ measuring the current-voltage (I-V) in a photodetector device that is illustrated in **Figure 13a** [32]. The effect of the optical power densities under illumination at 505 nm in the I-V curves is plotted in **Figure 13b**. This device shows a photoresponse among the best ones reported for other perovskite-based photodetectors, even considering different geometries: 2D-MAPbI$_3$ [47, 48], thin films [49, 50], nanowires [51, 52], and networks [53]. Starting from I-V measurements using different wavelengths from alternative light sources, always keeping the same illumination power of 1 mW/cm^2, it is possible to calculate the wavelength responsivity spectrum of the photodetector, by using the next formula:

$$R = I_{ph}/P \qquad (4)$$

with R being the responsivity, I$_{ph}$ the generated photocurrent, and P the illumination power on the device. These data are illustrated in **Figure 13c**, they show a maximum in the responsivity (0.26 A/W) for light with wavelength of 505 nm, which is near the wavelength with maximum solar irradiance. **Figure 13d** plots the current through the device as a function of time with a fixed voltage under pulsed illumination. This illumination mode allows to characterize the response time of the photodetector, in this device <100 ms (limited by the experimental setup), which is comparable with values previously reported [47, 48, 54, 55].

6. Conclusions

This chapter reviews recent structural results on the CH$_3$NH$_3$(Br$_{1-x}$Cl$_x$)$_3$ series. The combination of SXRD and NPD has permitted to address issues related to phase transitions below RT, and the conformation of the CH$_3$NH$_3^+$ units within the inorganic cages, formed by corner-sharing PBX$_6$ octahedra. Interestingly, it was observed that the progressive localization of the organic units is not only achieved through a reduction in symmetry (from cubic to tetragonal, and finally to orthorhombic), but also simply as a consequence of the contraction of the cubic unit cells as the Cl contents increase. This can be interpreted as an evolution of the X—H hydrogen bonds, as previously observed from DFT calculations. In summary, we have contributed with novel experimental evidence that facilitates a more reasonable design of hybrid halide perovskites with tunable properties for solar cell technologies.

Acknowledgements

Conflict of interest

The authors declare no conflict of interest.

Author details

Carlos Alberto López[1,2]*, María Consuelo Alvarez-Galván[3], Carmen Abia[1,4], María Teresa Fernández-Díaz[4] and José Antonio Alonso[1]*

1 Instituto de Ciencia de Materiales de Madrid, CSIC, Madrid, Spain

2 Instituto de Investigaciones en Tecnología Química (INTEQUI), UNSL, CONICET, Facultad de Química, Bioquímica y Farmacia, UNSL, San Luis, Argentina

3 Instituto de Catálisis y Petroleoquímica, CSIC, Madrid, Spain

4 Institut Laue Langevin, Grenoble, France

*Address all correspondence to: calopez@unsl.edu.ar and ja.alonso@icmm.csic.es

IntechOpen

References

[1] Lee MM, Teuscher J, Miyasaka T, et al. Efficient hybrid solar cells based on meso-superstructured organometal halide perovskites. Science (80-). 2012;**338**:643-647

[2] Kojima A, Teshima K, Shirai Y, et al. Organometal halide perovskites as visible-light sensitizers for photovoltaic cells. Journal of the American Chemical Society. 2009;**131**:6050-6051

[3] Kim H-S, Lee C-R, Im J-H, et al. Lead iodide perovskite sensitized all-solid-state submicron thin film mesoscopic solar cell with efficiency exceeding 9%. Scientific Reports. 2012;**2**:591

[4] Ye M, Hong X, Zhang F, et al. Recent advancements in perovskite solar cells: Flexibility, stability and large scale. Journal of Materials Chemistry A. 2016;**4**:6755-6771

[5] Fan Z, Sun K, Wang J. Perovskites for photovoltaics: A combined review of organic–inorganic halide perovskites and ferroelectric oxide perovskites. Journal of Materials Chemistry A. 2015;**3**:18809-18828

[6] Green MA, Emery K, Hishikawa Y, et al. Solar cell efficiency tables (version 48). Progress in Photovoltaics: Research and Applications. 2016;**24**:905-913

[7] Noh JH, Im SH, Heo JH, et al. Chemical management for colorful, efficient, and stable inorganic–organic hybrid nanostructured solar cells. Nano Letters. 2013;**13**:1764-1769

[8] Sadhanala A, Deschler F, Thomas TH, et al. Preparation of single-phase films of CH3NH3Pb(I1–xBrx)3 with sharp optical band edges. Journal of Physical Chemistry Letters. 2014;**5**:2501-2505

[9] Eperon GE, Stranks SD, Menelaou C, et al. Formamidinium lead trihalide: A broadly tunable perovskite for efficient planar heterojunction solar cells. Energy & Environmental Science. 2014;**7**:982

[10] De Wolf S, Holovsky J, Moon S-J, et al. Organometallic halide perovskites: Sharp optical absorption edge and its relation to photovoltaic performance. Journal of Physical Chemistry Letters. 2014;**5**:1035-1039

[11] Stranks SD, Eperon GE, Grancini G, et al. Electron-hole diffusion lengths exceeding 1 micrometer in an organometal trihalide perovskite absorber. Science (80-). 2013;**342**: 341-344

[12] Xing G, Mathews N, Sun S, et al. Long-range balanced electron- and hole-transport lengths in organic-inorganic CH3NH3PbI3. Science (80-). 2013;**342**:344-347

[13] Han Y, Meyer S, Dkhissi Y, et al. Degradation observations of encapsulated planar CH₃NH₃PbI₃ perovskite solar cells at high temperatures and humidity. Journal of Materials Chemistry A. 2015;**3**:8139-8147

[14] Yang J, Siempelkamp BD, Liu D, et al. Investigation of CH₃NH₃PbI₃ degradation rates and mechanisms in controlled humidity environments using in situ techniques. ACS Nano. 2015;**9**:1955-1963

[15] Akbulatov AF, Frolova LA, Dremova NN, et al. Light or heat: What is killing lead halide perovskites under solar cell operation conditions? Journal of Physical Chemistry Letters. 2020;**11**:333-339

[16] Senocrate A, Kim GY, Grätzel M, et al. Thermochemical stability of hybrid halide perovskites. ACS Energy Letters. 2019;**4**:2859-2870

[17] Kedem N, Brenner TM, Kulbak M, et al. Light-induced increase of electron

diffusion length in a p–n junction type CH3NH3PbBr3 perovskite solar cell. Journal of Physical Chemistry Letters. 2015;**6**:2469-2476

[18] Talbert EM, Zarick HF, Orfield NJ, et al. Interplay of structural and compositional effects on carrier recombination in mixed-halide perovskites. RSC Advances. 2016;**6**:86947-86954

[19] Sheng R, Ho-Baillie A, Huang S, et al. Methylammonium lead bromide perovskite-based solar cells by vapor-assisted deposition. Journal of Physical Chemistry C. 2015;**119**:3545-3549

[20] Zheng X, Chen B, Wu C, et al. Room temperature fabrication of CH3NH3PbBr3 by anti-solvent assisted crystallization approach for perovskite solar cells with fast response and small J–V hysteresis. Nano Energy. 2015;**17**:269-278

[21] Arora N, Orlandi S, Dar MI, et al. High open-circuit voltage: Fabrication of formamidinium lead bromide perovskite solar cells using fluorene–dithiophene derivatives as hole-transporting materials. ACS Energy Letters. 2016;**1**:107-112

[22] Edri E, Kirmayer S, Cahen D, et al. High open-circuit voltage solar cells based on organic–inorganic lead bromide perovskite. Journal of Physical Chemistry Letters. 2013;**4**:897-902

[23] Heo JH, Song DH, Im SH. Planar $CH_3NH_3PbBr_3$ hybrid solar cells with 10.4% power conversion efficiency, fabricated by controlled crystallization in the spin-coating process. Advanced Materials. 2014;**26**:8179-8183

[24] Zarick HF, Boulesbaa A, Puretzky AA, et al. Ultrafast carrier dynamics in bimetallic nanostructure-enhanced methylammonium lead bromide perovskites. Nanoscale. 2017;**9**:1475-1483

[25] Swainson IP, Hammond RP, Soullière C, et al. Phase transitions in the perovskite methylammonium lead bromide, $CH_3ND_3PbBr_3$. Journal of Solid State Chemistry. 2003;**176**:97-104

[26] Mashiyama H, Kawamura Y, Kasano H, et al. Disordered configuration of methylammonium of $CH_3NH_3PbBr_3$ determined by single crystal neutron diffractometry. Ferroelectrics. 2007;**348**:182-186

[27] Baikie T, Barrow NS, Fang Y, et al. A combined single crystal neutron/X-ray diffraction and solid-state nuclear magnetic resonance study of the hybrid perovskites $CH_3NH_3PbX_3$ (X = I, Br and Cl). Journal of Materials Chemistry A. 2015;**3**:9298-9307

[28] Maculan G, Sheikh AD, Abdelhady AL, et al. $CH_3NH_3PbCl_3$ single crystals: Inverse temperature crystallization and visible-blind UV-photodetector. Journal of Physical Chemistry Letters. 2015;**6**:3781-3786

[29] Rana S, Awasthi K, Bhosale SS, et al. Temperature-dependent electroabsorption and electrophoto-luminescence and exciton binding energy in $MAPbBr_3$ perovskite quantum dots. Journal of Physical Chemistry C. 2019;**123**:19927-19937

[30] Gao Z-R, Sun X-F, Wu Y-Y, et al. Ferroelectricity of the orthorhombic and tetragonal $MAPbBr_3$ single crystal. Journal of Physical Chemistry Letters. 2019;**10**:2522-2527

[31] Comin R, Walters G, Thibau ES, et al. Structural, optical, and electronic studies of wide-bandgap lead halide perovskites. Journal of Materials Chemistry C. 2015;**3**:8839-8843

[32] López CA, Martínez-Huerta MV, Alvarez-Galván MC, et al. Elucidating the methylammonium (MA) conformation in $MAPbBr_3$ perovskite with application in solar cells. Inorganic Chemistry. 2017;**56**:14214-14219

[33] Alvarez-Galván MC, Alonso JA, López CA, et al. Crystal growth, structural phase transitions, and optical gap evolution of $CH_3NH_3Pb(Br_{1-x}Cl_x)_3$ perovskites. Crystal Growth & Design. 2018;**19**(2):918-924. DOI: 10.1021/acs.cgd.8b01463

[34] López CA, Álvarez-Galván MC, Martínez-Huerta MV, et al. Dynamic disorder restriction of methylammonium (MA) groups in chloride–doped MAPbBr3 hybrid perovskites: A neutron powder diffraction study. Chemistry: A European Journal. 2019;**25**:4496-4500

[35] Poglitsch A, Weber D. Dynamic disorder in methylammonium-trihalogenoplumbates (II) observed by millimeter-wave spectroscopy. The Journal of Chemical Physics. 1987;**87**:6373-6378

[36] Chi L, Swainson I, Cranswick L, et al. The ordered phase of methylammonium lead chloride $CH_3ND_3PbCl_3$. Journal of Solid State Chemistry. 2005;**178**:1376-1385

[37] Varadwaj A, Varadwaj PR, Marques HM, et al. Halogen in materials design: Revealing the nature of hydrogen bonding and other non-covalent interactions in the polymorphic transformations of methylammonium lead tribromide perovskite. Materials Today Chemistry. 2018;**9**:1-16

[38] Li J, Rinke P. Atomic structure of metal-halide perovskites from first principles: The chicken-and-egg paradox of the organic-inorganic interaction. Physical Review B. 2016;**94**: 045201

[39] Leguy AMA, Goñi AR, Frost JM, et al. Dynamic disorder, phonon lifetimes, and the assignment of modes to the vibrational spectra of methylammonium lead halide perovskites. Physical Chemistry Chemical Physics. 2016;**18**:27051-27066

[40] Frost JM, Walsh A. What is moving in hybrid halide perovskite solar cells? Accounts of Chemical Research. 2016;**49**:528-535

[41] Yin T, Fang Y, Fan X, et al. Hydrogen-bonding evolution during the polymorphic transformations in $CH_3NH_3PbBr_3$: Experiment and theory. Chemistry of Materials. 2017;**29**:5974-5981

[42] Bernasconi A, Page K, Dai Z, et al. Ubiquitous short-range distortion of hybrid perovskites and hydrogen-bonding role: The MAPbCl₃ case. Journal of Physical Chemistry C. 2018;**122**:28265-28272

[43] Shimamura K, Hakamata T, Shimojo F, et al. Rotation mechanism of methylammonium molecules in organometal halide perovskite in cubic phase: An ab initio molecular dynamics study. The Journal of Chemical Physics. 2016;**145**:224503

[44] Tablero CC. The effect of the halide anion on the optical properties of lead halide perovskites. Solar Energy Materials & Solar Cells. 2019;**195**: 269-273

[45] Endres J, Egger DA, Kulbak M, et al. Valence and conduction band densities of states of metal halide perovskites: A combined experimental-theoretical study. Journal of Physical Chemistry Letters. 2016;**7**:2722-2729

[46] Ong KP, Wu S, Nguyen TH, et al. Multi band gap electronic structure in $CH_3NH_3PbI_3$. Scientific Reports. 2019;**9**:2144

[47] Wang G, Li D, Cheng H-C, et al. Wafer-scale growth of large arrays of perovskite microplate crystals for functional electronics and optoelectronics. Science Advances. 2015;**1**:e1500613

[48] Liu J, Xue Y, Wang Z, et al. Two-dimensional $CH_3NH_3PbI_3$

perovskite: Synthesis and optoelectronic application. ACS Nano. 2016;**10**:3536-3542

[49] Zhang Y, Du J, Wu X, et al. Ultrasensitive photodetectors based on island-structured $CH_3NH_3PbI_3$ thin films. ACS Applied Materials & Interfaces. 2015;**7**:21634-21638

[50] Lu H, Tian W, Cao F, et al. A self-powered and stable all-perovskite photodetector-solar cell nanosystem. Advanced Functional Materials. 2016;**26**:1296-1302

[51] Deng H, Dong D, Qiao K, et al. Growth, patterning and alignment of organolead iodide perovskite nanowires for optoelectronic devices. Nanoscale. 2015;**7**:4163-4170

[52] Zhuo S, Zhang J, Shi Y, et al. Self-template-directed synthesis of porous perovskite nanowires at room temperature for high-performance visible-light photodetectors. Angewandte Chemie International Edition. 2015;**54**:5693-5696

[53] Deng H, Yang X, Dong D, et al. Flexible and semitransparent organolead triiodide perovskite network photodetector arrays with high stability. Nano Letters. 2015;**15**:7963-7969

[54] Li D, Dong G, Li W, et al. High performance organic-inorganic perovskite-optocoupler based on low-voltage and fast response perovskite compound photodetector. Scientific Reports. 2015;**5**:7902

[55] Dong R, Fang Y, Chae J, et al. High-gain and low-driving-voltage photodetectors based on organolead triiodide perovskites. Advanced Materials. 2015;**27**:1912-1918